

Supplemental analysis material in support of
Methane depletion in both polar regions of Uranus inferred from HST/STIS
and Keck/NIRC2 observations

by

L. A. Sromovsky, E. Karkoschka, P. M. Fry, H. B. Hammel, I. de Pater, and K. Rages

1 Description of data reduction procedures.

Starting with flat-fielded science images, fringe flats, and WAVECALs from the STScI STIS data processing pipeline, the following steps are taken to produce a cube of geometrically and radiometrically calibrated monochromatic images of Uranus. These procedures are based on those developed by Karkoschka and Tomasko (2009) in processing 2002 STIS observations.

(1) *Interpolation of bad pixels and cosmic ray hits.* First, images were cleaned of pixels affected by cosmic rays and other defects. An automated routine found 44,000 bad pixels. These were checked to verify that the routine never found any real features. However, along the edges of big cosmic ray events, sometimes covering 100 pixels, the routine is conservative. If slightly elevated counts can be real, they are identified as good pixels and thus used to interpolate across the bad pixels, which then end up with counts 1 or 2 sigma above the background.

(2) *Flat-fielding.* Long wavelength fringing must be removed from G750L spectral images via division by normalized fringe flats (taken contemporaneously with Uranus science observations). For the “red” wavelength range (covered by the 750L grating), the two acquired flat-fields were averaged and the slow wavelength dependent variation was taken out. This gave the fringes and the variation due to variable slit width along the slit. This flat field was used for the red-range data. Averaging in wavelength was used to obtain the slit variation only and we shifted it vertically (along the slit) by almost one pixel to obtain a flat field for the “blue” wavelength range, which is not affected by fringing. Remaining east-west streaks (perpendicular to the slit) for the blue range were measured, and the blue flat field was changed by 0.1% RMS. There are still very low-contrast streaks remaining, but the results are considered acceptable. A correction is then applied for slit throughput as a function of image row.

(3) *Charge transfer efficiency corrections.* Next a column-by-column deconvolution is performed to correct for Charge Transfer Efficiency (CTE) losses. The previous method of KT2009 was used but the

charge loss was adjusted so that resulting images would show counts in space that were roughly symmetric (above and below Uranus). We did not achieve perfect symmetry for all wavelengths simultaneously since charge transfer is very complicated. The basics of the effect are summarized in the following. The signal collected by each pixel of a CCD is read out sequentially from top to bottom, with charge from each pixel transferred to the next until all pixel charges are transferred to a shift register at the bottom of the chip. A shortcoming of CCD detectors is that the efficiency of transferring charge is typically ~ 0.99995 instead of 1.00000. The consequence of this is that a point source imaged at the top of the chip will appear to be fainter than a point source imaged at the bottom, since some of the charge is lost (or trapped) during the readout. The other aspect of the CTE effect is that faint sources are more affected than bright ones. Thus, to obtain the correct relationship between the planet's disk and the surrounding "sky" background, which is due to the telescope PSF under ideal conditions, the sky background must be corrected for CTE effects. The closer to the readout, the less correction is needed, so the greater the accuracy of the correction. For this reason our 2012 STIS observations used the E1 aperture, which is close to the readout amplifiers. This issue was present for both 2002 and 2012 observations.

(4) *Scattered light corrections.* A spectral image deconvolution was performed to reduce the effects of the "Red Halo" CCD substrate scattering, again following KT2009.

(5) *Distortion correction.* Spectral lines are curved and not vertical, and spectra of the same location are curved and not horizontal. This distortion was removed according to published STScI parameters (Bostroem and Proffitt 2011), except that the first-order terms were adjusted according to measurements on the 2012 spectral calibration data.

(6) *Spectral calibration.* Zero- and first order terms of the function describing wavelength locations on the detector were measured for each exposure. Second-order terms were from STScI (Walsh et al. 2001). For the blue range, 7 Fraunhofer lines were measured, and they stayed constant within 0.01 pixel RMS for the 13 exposures. For the red range, 2 Fraunhofer lines were measured, and they moved by 0.12 pixels (0.06 nm) within the two hours. The red shift due to rotation of Uranus was taken into account based on the location probed, due to the changing distance Earth-Uranus, and due to HST's orbit around Earth. Vacuum wavelengths were used for calibration (since HST is in vacuum). Note that the longest wavelength sharp spectral feature measurable is the H-alpha Fraunhofer line. Thus, much beyond 656 nm, the wavelength calibration is not as reliable as below. However, since spectral features at long wavelengths are not very sharp (compared to short-wavelength Raman features, for example), it

is not as critical there.

(7) *Spectral resolution adjustment.* The blue range was smoothed and the red range was slightly sharpened (rapid variations with wavelength were enhanced) to obtain 1 nm resolution throughout. We took into account that spectra are sharper near the limb of Uranus because the slit is not evenly illuminated.

(8) *Navigation.* The red-range data were convolved with the spectral sensitivity distribution of the acquisition image and then each slit was moved in both axes to obtain the best fit. For the data far from the limb and central meridian, there is a linear trend in best-fit slit position up to about 0.04 pixels RMS (except a 0.2-pixel jump during occultation by Earth), which we adopted. This trend was then extrapolated toward the central meridian and toward the limb because navigation there is less accurate. Finally, the red-range navigation was adjusted using data in deep methane bands, where the bright ring around the limb allows accurate navigation. Navigation of the blue range was done by comparing profiles with the red range in the overlapping spectral region.

(9) *Interpolation of blue range.* The same east-west interpolation was used as for the 2002 data to produce 0.05'' sampling from the 0.15'' east-west actual sampling. It is a cubic interpolation, near the center mostly east-west, near the limb mostly parallel to the limb.

(10) *Spatial resampling.* The data cube has 1800 wavelengths from 300.4 to 1020 nm and 75×150 pixels spaced by $0.015 \times R_U$, where $R_U = 25559$ km, the equatorial radius of Uranus (Seidelmann et al. 2002). This provides an angular scale $0.0277''/\text{pixel}$ compared to the along-slit pixel scale of 0.05'' and the $0.0569''$ per scan step from center to limb. This sub-sampling was used to reduce quantization errors associated with pointing changes during spatial scans. It also matches the sub-sampling used by KT2009 and thus facilitates direct comparisons. The right-most column goes along the central meridian, and the 75th pixel counting from the south is the center of the disk. Cubic interpolation was used throughout.

(11) *Deconvolution of PSF.* A final deconvolution is then performed to reduce the effects of the telescope diffraction, using monochromatic PSFs generated by Tiny Tim (Krist 1995), with an adjustment to correct for lower sample frequency in the slit stepping direction. The Tiny-Tim PSF was used for each wavelength to take out features of the HST PSF. The deconvolved images should have the same PSF for all wavelengths shown in Table 1, where all counts add up to 100,000. This PSF is for the final data sampled at 0.015×25559 km (the equatorial radius R_U of Uranus). Model I/Fs with $0.015 R_U$ sampling and convolved with this PSF should be comparable to the deconvolved spectral data cube provided in

supplemental material.

We combined blue and red ranges using the same method as for the 2002 data; we used the blue-range shortward of 530 nm and the red-range longward of 540 nm, with a linearly sliding weighted average in between.

Table 1: Point spread function (PSF) for final calibrated data cube.

0	0	-11	-22	-20	-22	-11	0	0
0	-19	55	400	615	400	55	-19	0
-11	55	894	2370	3168	2370	894	55	-11
-22	400	2370	5458	7058	5458	2370	400	-22
-20	615	3168	7058	9048	7058	3168	615	-20
-22	400	2370	5458	7058	5458	2370	400	-22
-11	55	894	2370	3168	2370	894	55	-11
0	-19	55	400	615	400	55	-19	0
0	0	-11	-22	-20	-22	-11	0	0

2 End-to-end comparisons of STIS with WFC3 support images

As a sanity check on the STIS processing we compared line scans across WFC3 images to the corresponding scans across synthetic WFC3 images created from our calibrated STIS data cube. The results shown in Fig. 1 demonstrate overall excellent agreement. The worst discrepancy is for the FQ937N filter, which deviates by 10 % from our adopted STIS calibration, reasons for which are discussed in the main text. Also notable is the FQ727N comparison at $\mu = 0.3$, for which the WFC3 image has somewhat less limb brightening than our STIS-synthesized image. These discrepancies have no significant impact on our science results.

3 Further discussion of center-to-limb fitting results

The true center-to-limb profile is depressed near the limb by the blur of the imaging system. To avoid having to create, for every model calculation, a synthetic disk that could then be convolved with the imaging system PSF so that a model could be compared with the observed profile, we instead applied a crude correction. We created a synthetic planetary disk of unit I/F, convolved that disk with the PSF

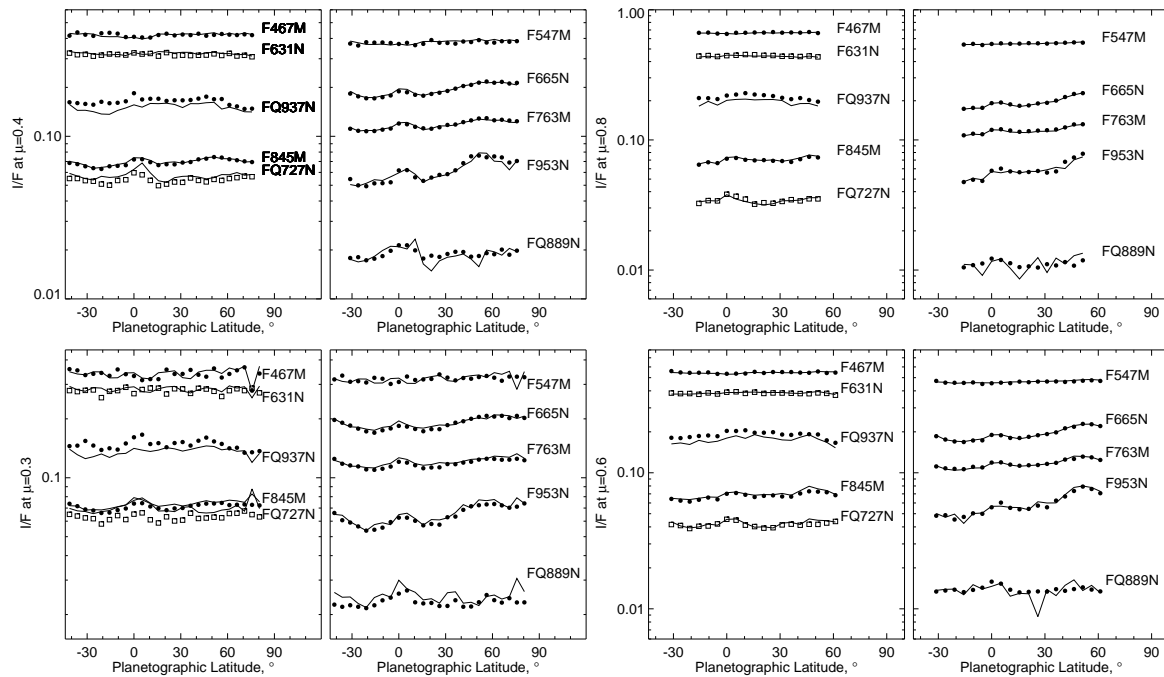


Figure 1: Comparison of WFC3 (symbols) and STIS synthetic WFC3 (lines) vs. latitude at fixed solar zenith angle cosines of 0.3 (LL), 0.4 (UL), 0.6 (LR), and 0.8 (UR), for each of the 11 filters used. These I/F values are obtained from the synthetic images by unsmoothed interpolation, and slightly different results would be obtained from CTL fits described in the text.

kernel used in reconvolving the deconvolved measured images, then computed the ratio of the perfect disk to the convolved synthetic disk. That produced a correction factor, which we applied to the observed I/F values prior to carrying out fits to each center-to-limb profile. The correction is negligible for zenith angle cosines greater than or equal to 0.3.

Center-to-limb fitting took approximate account of the two-way transmission of the rings of Uranus, which produces about a 1.5% depression in I/F at the center of the epsilon ring (this depression can be barely seen in the F467M image in Fig. 3 of the main text). We determined a correction function to reduce the ring's obscuration effects on center-to-limb fits. We started with a simulated F467M image, produced by a weighted average of monochromatic STIS images, as described in the main text. A ring transmission map was created by starting with all pixels set to unity. The pixels at the ring location (French et al. 1986) were set to a trial transmission value then the map was blurred with a Gaussian of a trial FWHM value. The simulated F467M image was then divided by this correction image. The ring transmission and FWHM values were empirically adjusted until the ring was no longer visible in a high-pass filtered version of the F467M image. The best fit values were roughly 0.935 and 4.5

pixels respectively. We ignored reflecting ring light because ring albedo is so low that reflected light contributions are not apparent at CCD wavelengths.

Sample fits at six latitudes from 45° S to 80° N are provided in Figs. 2. Most of the scatter about the fitted profiles is due to noise, which is often amplified by the deconvolution process. The exception appears at 41° N where a large deviation near $\mu=0.87$ is produced by a small discrete cloud feature. Because the range of observed μ values decreases away from the equator at high southern and northern latitudes, latitudinal comparisons at high μ values in those regions rely on uncertain extrapolations.

The CTL fits can also be used to create zonally smoothed images by replacing the observed I/F for each pixel by the fitted value. Results of that procedure are displayed for seven sample wavelengths in Fig. 3. Note that the image for the H₂ CIA dominated wavelength (826.8 nm) shows much more equator-to-pole darkening than the images for the methane-dominated or methane-only wavelengths, implying that there is relatively less methane absorption (compared to H₂ absorption) at high latitudes. This implication is based on the fact that these wavelengths are roughly sensitive to the same pressure range and thus are not sensing grossly different aerosol contributions.

4 Comparisons of latitudinal profiles at continuum wavelengths

Fig. 4 compares 2002 and 2012 scans at continuum wavelengths. The 2002 values were multiplied by 0.98 to provide the best match with 2012 values where they overlap.

5 Further discussion of the simplified model of CH₄ /H₂ variations

Sample fits of the 815–835 nm spectra at additional latitudes not shown in the main text are provided in Fig. 5 for comparison with previously shown latitudes. The fit at lower latitudes is generally not as good as at high latitudes. The latitude dependence of fit quality can vary depending on how the model is used, and there are many options that were investigated. Different zenith angle choices lead to somewhat different results; in fact using small μ values provides improved fit quality relative to larger values, but these samples don't reach as deeply into the atmosphere. It is also possible to make slightly more complicated models, fitting the effective temperature of hydrogen at each latitude, for example. When that is done under the assumption that the para fraction is at equilibrium, the temperature varies with latitude from about 75 K at high northern latitudes to about 90 K at high southern latitudes. In this case the temperature varies on a small scale, which may be responsible for the small scale variations

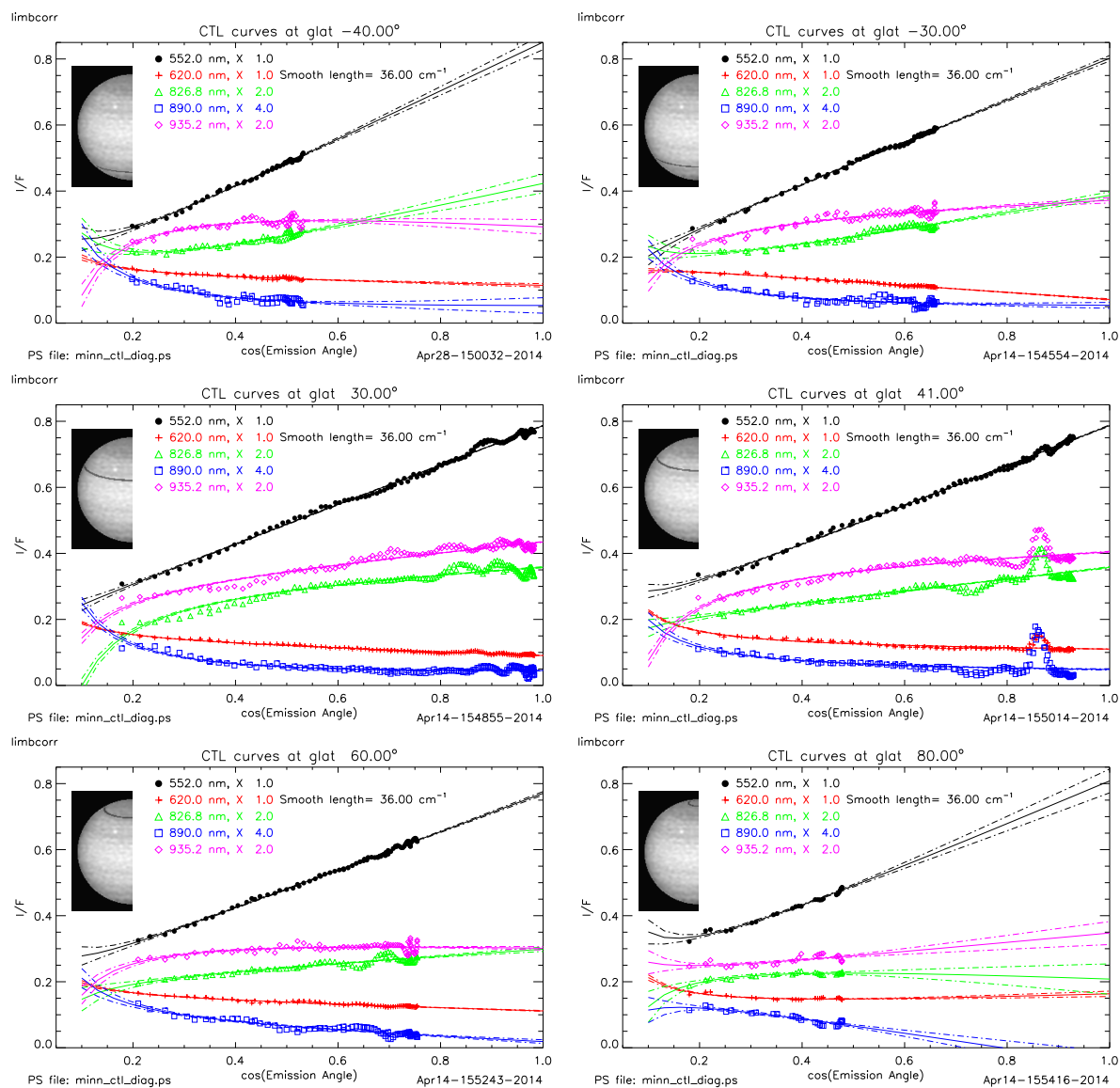


Figure 2: Sample center-to-limb fits at six different latitudes as described in the main text. Each panel shows STIS I/F samples and fit lines with uncertainty bands for five different wavelengths indicated in the legends. In each panel the latitude band sampled for each fit is darkened in the inset image of the half-disk of Uranus. Note that the fits for 41° N are not much disturbed by the cloud feature near $\mu=0.87$.

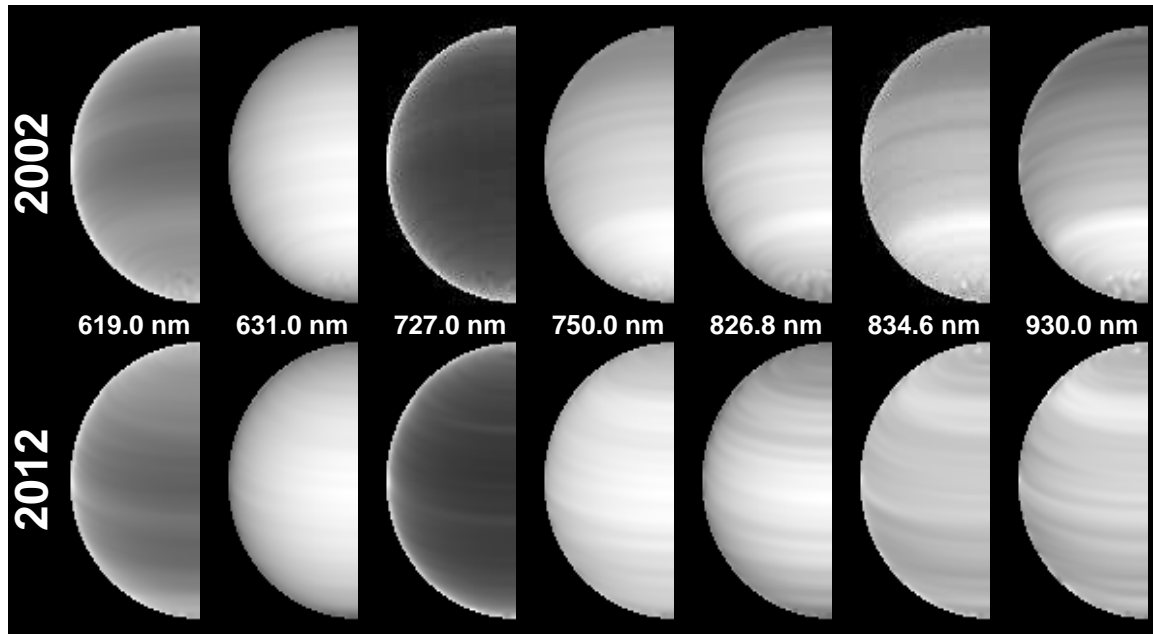


Figure 3: Comparison of 2002 and 2012 synthetic images created from CTL fits for seven sample wavelengths (these are auto-scaled). Note that the images for the H₂ CIA-dominated wavelength (826.8 nm) have relatively bright low latitudes and darker polar regions, while the images for the methane-dominated wavelength of 834.6 nm, and the methane-only wavelength of 930 nm, do not. This implies that there is relatively less methane absorption (compared to H₂ absorption) at high latitudes. Note that the longitudinal structure seen near the poles, a region where CTL fits did not replace the original image data, is mostly due to noise.

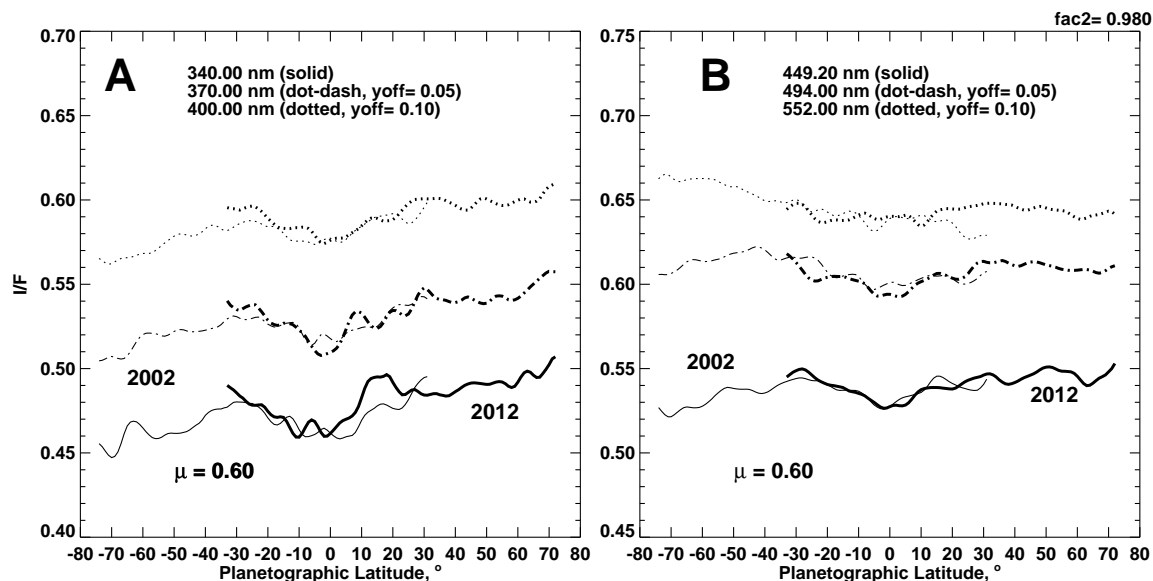


Figure 4: I/F vs latitude for six continuum wavelengths indicated in the legends. Thick curves are for 2012 and thin curves for 2002. These are plots of center-to-limb fitted values instead of raw image data. The 2002 I/F values were multiplied by 0.98 to provide the best match with 2012 values in the overlap region. Most of the change seen at continuum wavelengths is likely due to calibration differences between 2002 and 2012.

of the hydrogen absorption term seen in the simpler model. It is also possible to fit both the effective temperature of CIA absorption and the para fraction. This allows for much improved fit quality at low latitudes, resulting in generally higher effective temperatures, but higher para fractions that are more compatible with much lower temperatures. This could only be obtained by downward mixing of the higher stratospheric para fractions at all latitudes, which is not plausible. To obtain a best fit para fraction that is in thermal equilibrium, the effective temperature needs to be near 80 K. We decided to stick with the simpler model as a crude means of interpolating between latitudes where full radiation transfer models provide more reliable tie points.

6 Comparison of high-latitude methane variations with Keck imaging.

To further evaluate the possibility that the high latitude variations in effective methane VMR are real, we looked for some evidence of a similar pattern in the high-resolution near-IR Keck images from 2012. These are much more sensitive to cloud structure due to use of longer wavelengths and higher spatial resolution (often reaching 0.06 arcseconds). Initially we suspected that latitude bands with more “con-

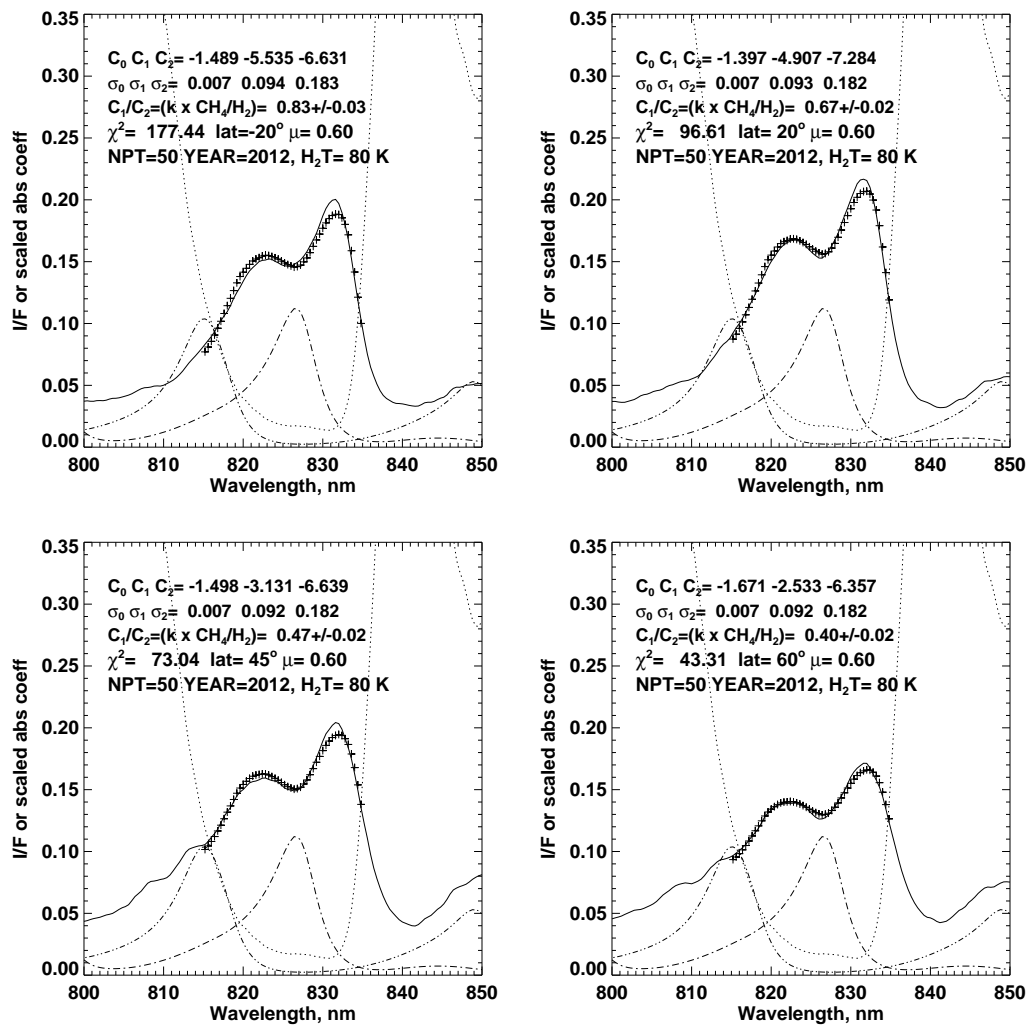


Figure 5: The 2012 I/F spectrum (solid curves) from 815 to 835 nm at $\mu=0.6$ for four sample latitudes (-20°, 20°, 45°, and 60° from left to right and top to bottom), using the simplified model (+) of Eq. 2 given in the main text. Also shown are relative variations of absorption by methane (dotted) and H₂ (dot-dash for para and double-dot-dash for ortho).

vective” cloud features might be correlated with regions of upwelling and thus increased methane VMR values. To test this idea we started with H-band Keck images from 16 August 2012 and 4 November 2012 (before and after our STIS observations). These were mosaicked to form high signal-to-noise ratio images using techniques described by Fry et al. (2012). These were high-pass filtered to enhance the contrast of faint cloud features, then zonally averaged over 90° in longitude to define any latitudinal pattern that might be present at high northern latitudes.

The comparison results are shown in Fig. 6. We found significant correlations between the zonal

mean cloud variations and the zonal mean methane VMR variations over the 55° N to 82° N latitudinal range. But the correlation surprised us in being negative instead of positive. Correlation coefficients for the two sets of variations are -0.552 for 15 August (significant at the 12 % level) and -0.513 (significant at the 10 % level) for 4 November, or -0.683 (significant at the 8 % level) for 4 November if STIS results are shifted 1° N (a similar shift for the 15 August results produces little change in the correlation coefficient). The significance levels quoted are the probabilities that two sets of 7 normally distributed random variables could produce correlations this negative (or more negative). We used seven as the approximate number of independent STIS spatial samples over the latitude range of interest. The actual significance is slightly higher because the Keck spatial resolution is somewhat higher than that of the STIS images. A possible physical interpretation of the anticorrelation is that where the effective methane amount is reduced, the cloud features become more visible due to reduced absorption above the clouds. The depth of these small high-latitude cloud features is roughly constrained by 2011 observations in H and Hcont filters, from which Sromovsky et al. (2012) found that most were deeper than the methane condensation level, many near 2 bars, under the assumption of no methane depletion and using the F1 structure and methane profile. If we account for the methane depletion at high latitudes, these pressure estimates would increase, and thus might be below the level of significant depletion.

It is also worth noting that the pattern of high-latitude cloud brightness variations in the Keck images north of 55° N is relatively stable over time, when averaged over longitude. Both 16 August and 4 November 2012 images show similar patterns in Fig. 6, with larger amplitudes present in the 4 November image, probably due to better seeing conditions on the night these images were acquired. We also found similar patterns in Keck/NIRC2 H-band images acquired on 25 July 2012 and 15 August 2013. While some details of the pattern do vary, the location of minima seem to be relatively unchanged over at least a year.

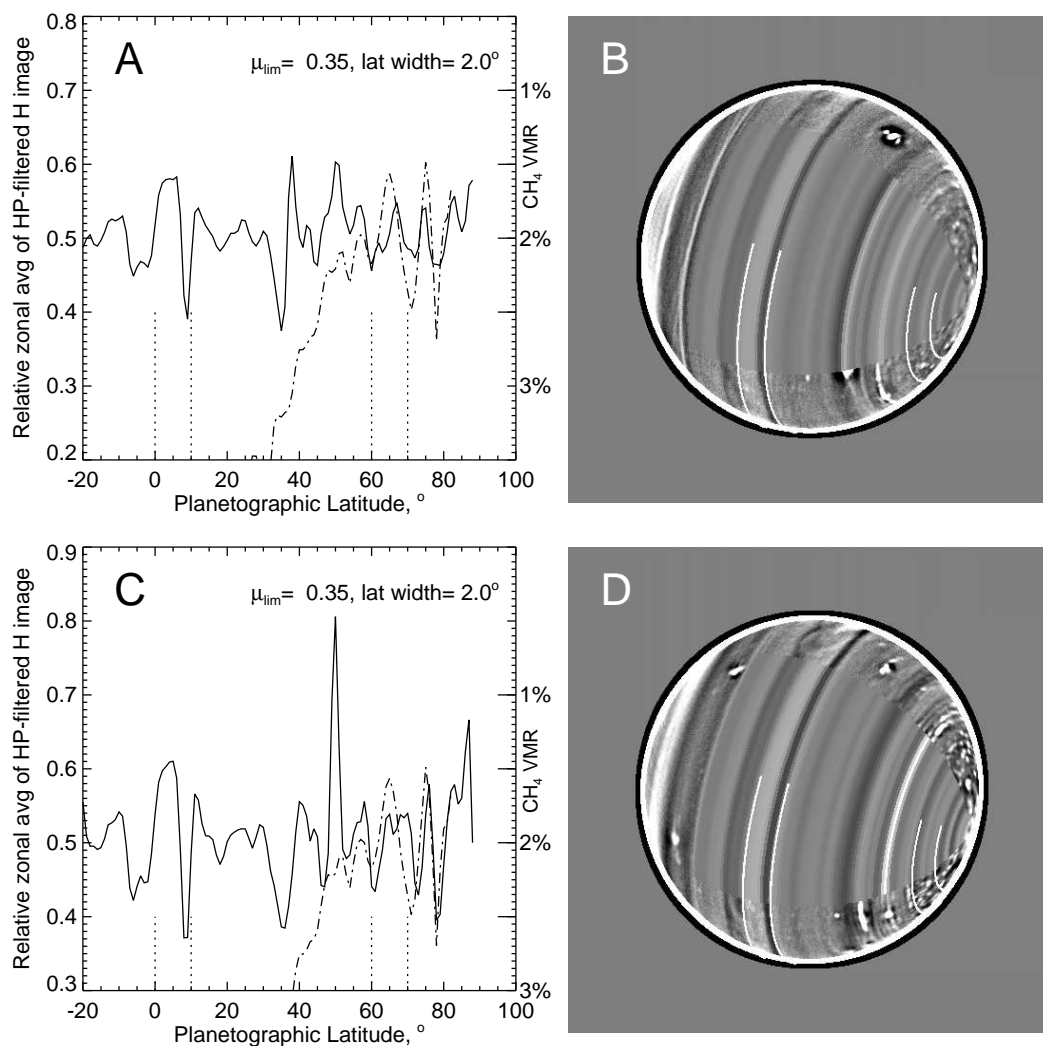


Figure 6: Effective STIS-derived methane mixing ratio vs. latitude profile (dot-dash curves in A, C) from Fig. 12A of the main text compared to relative zonal averages (solid curves in A, C) of high-pass filtered high signal-to-noise H-band ($1.62 \mu\text{m}$) Keck/NIRC2 images from 16 August 2012 (B) and 4 November 2012 (D). In the images in B and D the 90° of pixels that were averaged have been replaced by their longitudinally averaged values. Grid lines at 0° , 10° , 60° , and 70° extend half way across the images in B and D, and vertical dotted lines mark the same latitudes in A and C. Correlations between zonal average variations and effective methane VMR variations from 55°N to 82°N are significant (see text).

7 Cloud model scattering properties

Many of our cloud model parameters are based on those of KT2009 (Karkoschka and Tomasko 2009). Their diffuse model (compared to our compact model in Fig. 7) has four layers of aerosols, the uppermost being a Mie-scattering stratospheric haze layer characterized by an optical depth at $0.9 \mu\text{m}$, a gamma size distribution Hansen (1971), with a mean radius of $a = 0.1 \mu\text{m}$ and a normalized variance of $b = 0.3$. These particles are assumed to have a real index of 1.4, and an imaginary index following the KT2009 relation

$$n_i(\lambda) = 0.055 \exp[(350 - \lambda)/100], \quad (1)$$

for λ in nm and is only applicable between 350 nm and 1000 nm (as are the subsequent equations). This upper haze was distributed vertically above the 100 mb level with a constant optical depth per bar. The remaining layers in the KT2009 model are characterized by a wavelength-independent optical depth per bar and a wavelength-dependent single-scattering albedo, given by

$$\bar{\omega}_r(\lambda) = 1 - 1/[2 + \exp[(\lambda - 290)/37]], \quad (2)$$

again for λ in nm. Their adopted double Henyey-Greenstein phase function for the tropospheric layers used $g_1 = 0.7$, $g_2 = -0.3$, and a wavelength-dependent fraction for the first term, given by

$$f_1(\lambda) = 0.94 - 0.47 \sin^4[(1000 - \lambda)/445], \quad (3)$$

which produces a backscatter that decreases with wavelength, as shown in Fig. 8. The three tropospheric layers are uniformly mixed with gas molecules, with different optical depths per bar in three distinct layers: 0.1-1.2 bars (upper troposphere), 1.2-2 bars (middle troposphere), and $P > 2$ bars (lower troposphere). These optical depths per bar parameters are the adjustable ones we use to fit this model to the observations.

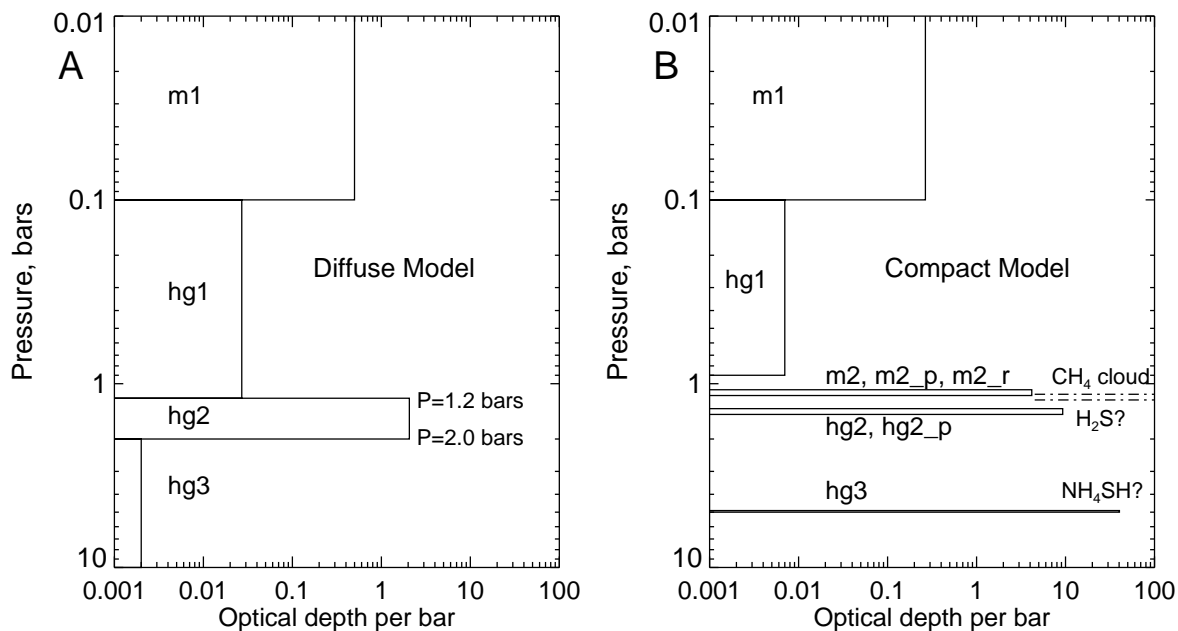


Figure 7: Diffuse (A) and compact (B) cloud model vertical structures. Compared to the KT2009, model, the compact model has two layers additional adjustable parameters of base pressure (for the new *hg2* layer) and base pressure and particle radius (for the new *m2* layer).

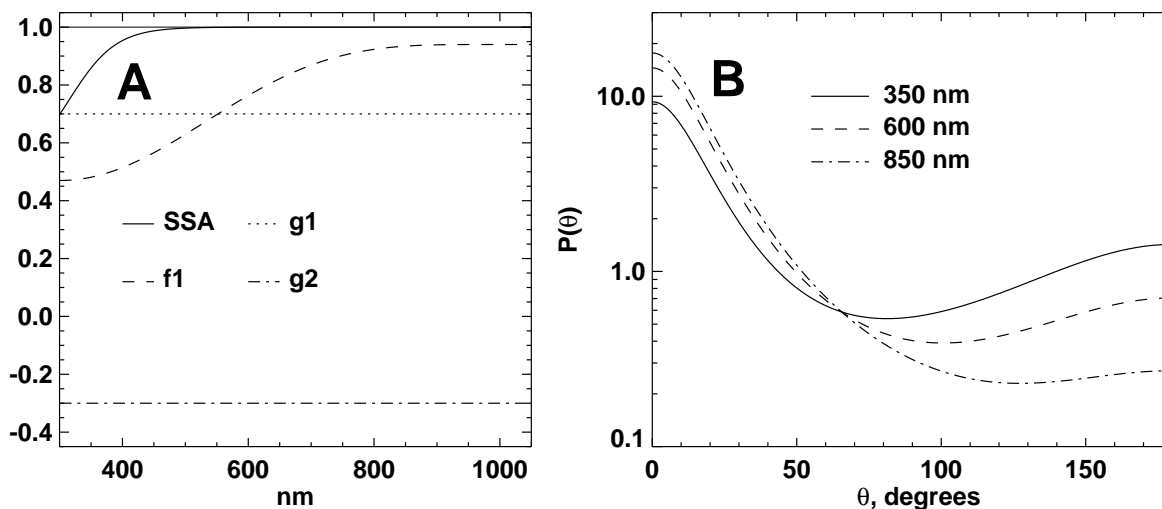


Figure 8: Wavelength dependent functions used in KT2009 cloud models (A) and sample phase functions derived from these parameters (B).

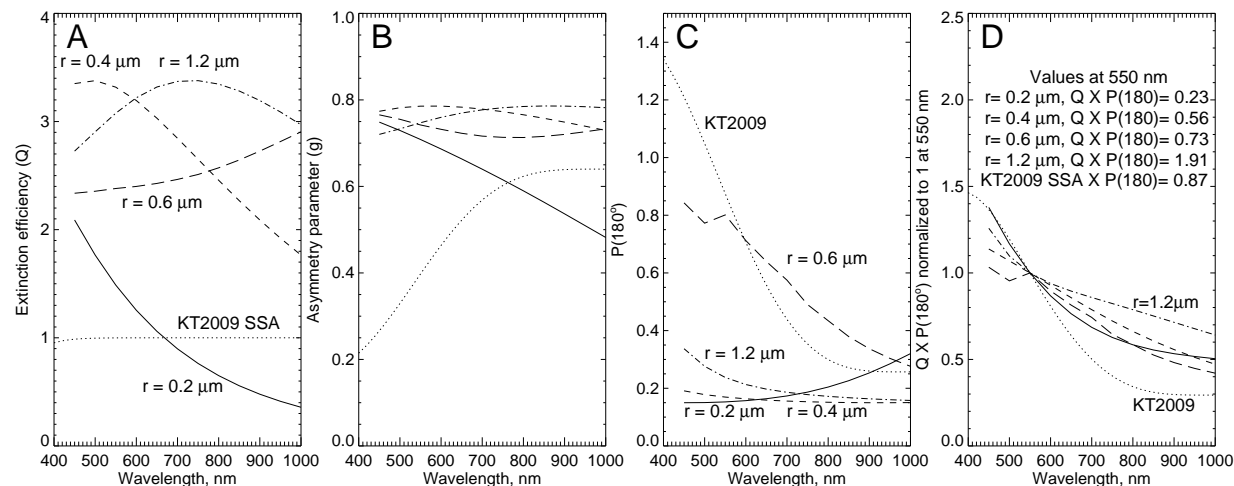


Figure 9: Mie particle scattering properties for four sizes of particles, $n=1.4+0i$, and a gamma size distribution of variance 0.1. Also shown are KT2009 single-scattering albedo (in A), asymmetry parameter (B), backscatter phase function (C) and backscatter efficiency normalized to unity at 550 nm (D).

The wavelength dependence of the extinction efficiency, asymmetry parameter, backscatter phase function, and backscatter efficiency, are given in Fig. 9 for the range of Mie particles we considered for the putative methane layer (the UMTC layer). We also show corresponding values for the KT2009 tropospheric particles, where applicable. The KT2009 tropospheric particles have wavelength independent optical depth, and thus the way its backscatter efficiency varies with wavelength is entirely determined by the phase function (defined by Eq. 3). For all the Mie particle sizes shown, there is a decline in backscatter efficiency with wavelength, but not as large as for the KT2009 tropospheric particles. For optically thin particle layers, the reflectivity of the layer is largely determined by the backscatter efficiency. For optically thick layers other aspects of the phase function are also important.

8 Layer contributions and comparison of modeled to measured spectra

A detailed comparison of a best-fit model spectral set (a spectrum at each of three different view angles) with the observed equatorial spectra used to constrain it is provided in Fig. 10. The relative roles played by each of the significant model layers in creating the observed spectral characteristics and the effect of the $m2$ layer particle size, are illustrated in Fig. 11B-F. The model shown is an undepleted F1 profile at the equator. The contribution of the $hg1$ layer is insignificant, and therefore not shown. In the difference spectra for different parameters we see different spectral shapes and different responses to view angle changes. This is what makes it possible to constrain the parameters in the fitting process. Recall that the

fits are done only over the 550 nm to 1000 nm spectral range, while these comparisons extend to 300 nm. In panel A, we show how the fit compares to the observed spectrum. Even below the wavelength range of the fit, the model and measured spectra are generally within 10% of each other, a difference that could be significantly reduced by modifying the single-scattering albedo function below 550 nm. Also note that the larger fractional errors in this comparison are at wavelengths where noise levels are substantial. This is more readily seen in Fig. 10, where spectral ratios are compared with expected uncertainties.

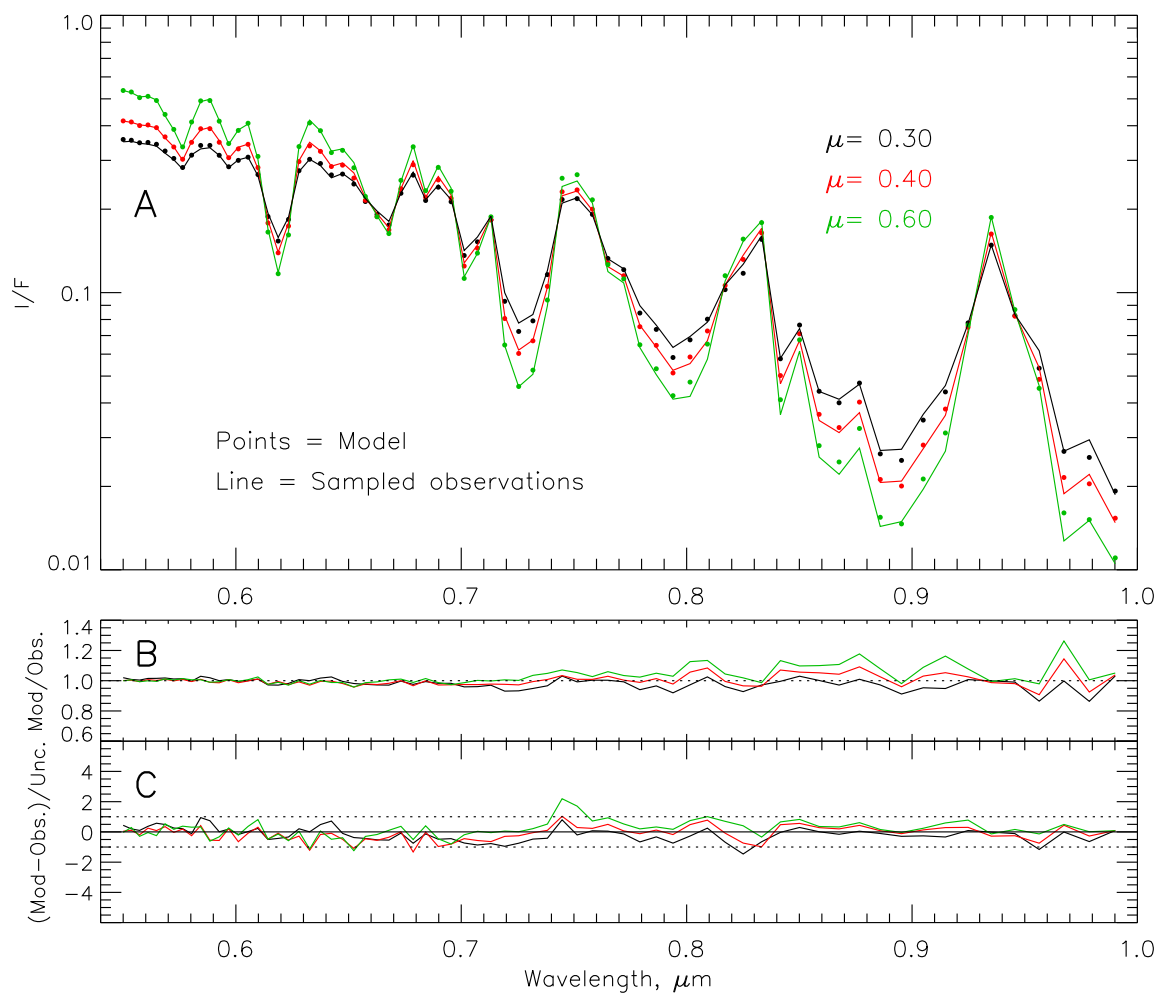


Figure 10: Comparison of model and measured spectra (A) at the equator, ratio of measured to model spectra (B) and difference spectra relative to expected uncertainty (C).

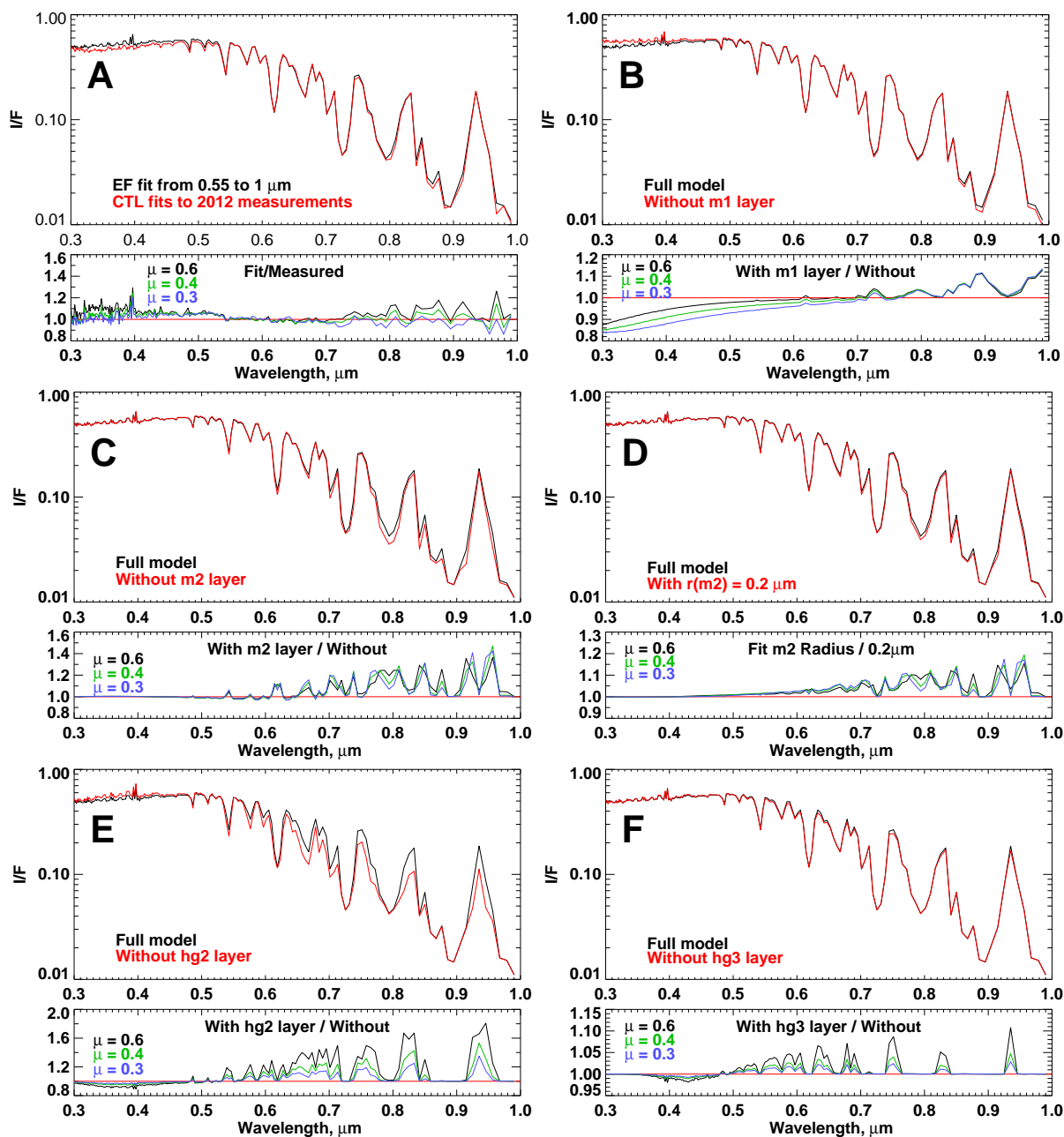


Figure 11: A: Comparison of measured STIS spectrum (red) at equator with a compact model fit (black) using the EF structure model, with spectra shown at a solar zenith angle cosine of 0.6 and ratios shown for all three cosine values); B-F: Comparisons of the model spectrum with spectra for same model with one aerosol layer removed or particle size changed (B: $m1$ removed, C: $m2$ removed, D: $m2$ particle radius reduced from $0.57 \mu\text{m}$ to $0.2 \mu\text{m}$, E: $hg2$ removed, F: $hg3$ removed).

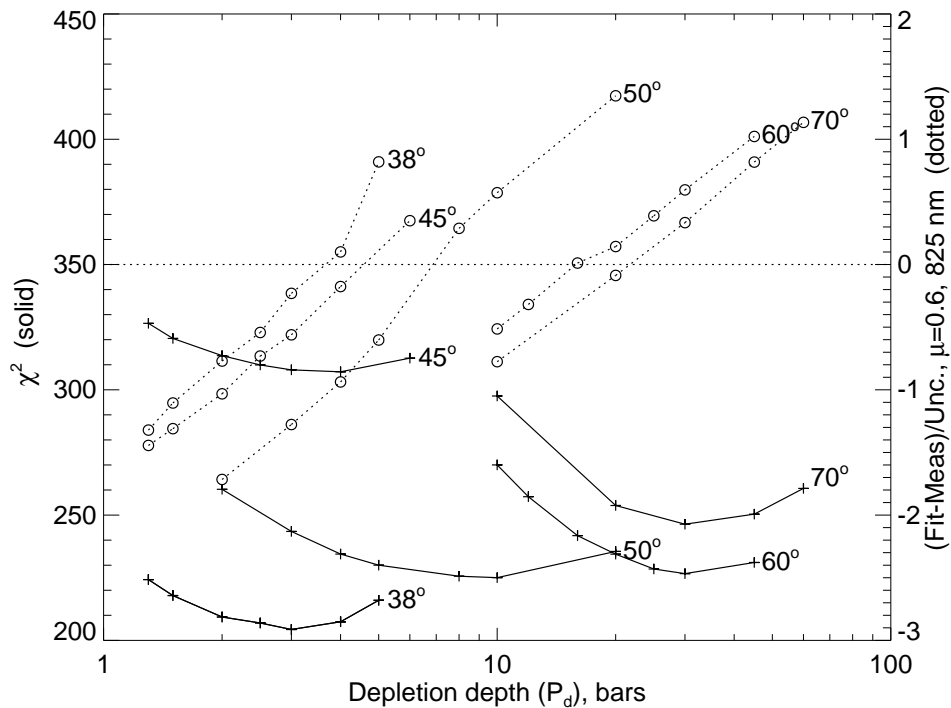


Figure 12: Fit quality estimates (χ^2 on left axis, 825-nm error on right) for compact cloud layer models versus depletion depth for depletion profiles with $\nu x = 3$.

9 Fit results for penetration depth versus latitude

The results for fits at 5 different latitudes for models with $\nu x=3$, as a function of penetration depth P_d are shown in Fig. 12. The reason for the relatively high χ^2 value for fits at 45° N is not understood. Fit quality was not improved using $\nu x=2$.

References

- Bostroem, K. A., Proffitt, C., 2011. STIS Data Handbook v. 6.0.
- French, R. G., Elliot, J. L., Levine, S. E., 1986. Structure of the Uranian rings. II - Ring orbits and widths. *Icarus* 67, 134–163.
- Fry, P. M., Sromovsky, L. A., de Pater, I., Hammel, H. B., Rages, K. A., 2012. Detection and Tracking of Subtle Cloud Features on Uranus. *Astron. J.* 143, 150–161.
- Hansen, J. E., 1971. Circular polarization of sunlight reflected by clouds. *Journal of Atmospheric Sciences* 28, 1515–1516.

- Karkoschka, E., Tomasko, M., 2009. The haze and methane distributions on Uranus from HST-STIS spectroscopy. *Icarus* 202, 287–309.
- Krist, J., 1995. Simulation of HST PSFs using Tiny Tim. In: Shaw, R. A., Payne, H. E., Hayes, J. J. E. (Eds.), *Astronomical Data Analysis Software and Systems IV*. Vol. 77 of *Astronomical Society of the Pacific Conference Series*. pp. 349–352.
- Seidelmann, P. K., Abalakin, V. K., Bursa, M., Davies, M. E., de Bergh, C., Lieske, J. H., Oberst, J., Simon, J. L., Standish, E. M., 2002. Report of the IAU/IAG Working Group on Cartographic Coordinates and Rotational Elements of the Planets and Satellites. *Celestial Mechanics and Dynamical Astronomy* 82, 83–110.
- Sromovsky, L. A., Fry, P. M., Hammel, H. B., de Pater, I., Rages, K. A., 2012. Post-equinox dynamics and polar cloud structure on Uranus. *Icarus* 220, 694–712.
- Walsh, J. R., Goudfrooij, P., Malumuth, E., 2001. STIS Geometric Distortion - SMOV3A tests for CCD, NUVMAMA and FUV-MAMA. Tech. rep.